

LoFormer: Local Frequency Transformer for Image Deblurring

Xintian Mao
Shanghai Key Laboratory of
Multidimensional Information
Processing
East China Normal University
Shanghai, China
52265904010@stu.ecnu.edu.cn

Jiansheng Wang
Shanghai Key Laboratory of
Multidimensional Information
Processing
East China Normal University
Shanghai, China
52191214001@stu.ecnu.edu.cn

Xingran Xie
Shanghai Key Laboratory of
Multidimensional Information
Processing
East China Normal University
Shanghai, China
51215904112@stu.ecnu.edu.cn

Qingli Li
Shanghai Key Laboratory of
Multidimensional Information
Processing
East China Normal University
Shanghai, China
qli@cs.ecnu.edu.cn

Yan Wang*
Shanghai Key Laboratory of
Multidimensional Information
Processing
East China Normal University
Shanghai, China
ywang@cee.ecnu.edu.cn

Abstract

Due to the computational complexity of self-attention (SA), prevalent techniques for image deblurring often resort to either adopting localized SA or employing coarse-grained global SA methods, both of which exhibit drawbacks such as compromising global modeling or lacking fine-grained correlation. In order to address this issue by effectively modeling long-range dependencies without sacrificing fine-grained details, we introduce a novel approach termed Local Frequency Transformer (LoFormer). Within each unit of LoFormer, we incorporate a Local Channel-wise SA in the frequency domain (Freq-LC) to simultaneously capture cross-covariance within low- and high-frequency local windows. These operations offer the advantage of (1) ensuring equitable learning opportunities for both coarse-grained structures and fine-grained details, and (2) exploring a broader range of representational properties compared to coarse-grained global SA methods. Additionally, we introduce an MLP Gating mechanism complementary to Freq-LC, which serves to filter out irrelevant features while enhancing global learning capabilities. Our experiments demonstrate that LoFormer significantly improves performance in the image deblurring task, achieving a PSNR of 34.09 dB on the GoPro dataset with 126G FLOPs. <https://github.com/DeepMed-Lab-ECNU/Single-Image-Deblur>

CCS Concepts

• Computing methodologies → Reconstruction.

*Corresponding author.

Permission to make digital or hard copies of all or part of this work for personal or classroom use is granted without fee provided that copies are not made or distributed for profit or commercial advantage and that copies bear this notice and the full citation on the first page. Copyrights for components of this work owned by others than the author(s) must be honored. Abstracting with credit is permitted. To copy otherwise, or republish, to post on servers or to redistribute to lists, requires prior specific permission and/or a fee. Request permissions from permissions@acm.org.
MM '24, October 28–November 1, 2024, Melbourne, VIC, Australia
© 2024 Copyright held by the owner/author(s). Publication rights licensed to ACM.
ACM ISBN 979-8-4007-0686-8/24/10
<https://doi.org/10.1145/3664647.3680888>

Keywords

self-attention, frequency domain, image deblurring

ACM Reference Format:

Xintian Mao, Jiansheng Wang, Xingran Xie, Qingli Li, and Yan Wang. 2024. LoFormer: Local Frequency Transformer for Image Deblurring. In *Proceedings of the 32nd ACM International Conference on Multimedia (MM '24)*, October 28–November 1, 2024, Melbourne, VIC, Australia. ACM, New York, NY, USA, 17 pages. <https://doi.org/10.1145/3664647.3680888>

1 Introduction

The field of image deblurring has made significant advances riding on the wave of global feature learning methods. Some MLP-based methods have been proposed, e.g., MAXIM [53] decomposes the global MLP operation into window-MLP and grid-MLP in a sparse manner (see Fig. 1(a)). In addition to MLP-based methods, recent research explorations [52, 55, 62] have shown the ability of Transformers in image deblurring task. Self-Attention (SA) [54], the key to capturing long-range dependency, has quadratic computational complexity *w.r.t.* the number of tokens, which is infeasible to be applied to high-resolution images in image deblurring. To make computation feasible, existing methods try various ways to reduce the number of tokens for SA in spatial domain, which can be categorized into three groups. (1) Local Spatial-wise SA (we use the abbreviation Spa-LS to represent **S**patial domain-**L**ocal **S**patial-wise SA). Uformer [55] proposes a local-enhanced window Transformer block to capture local context (see Fig. 1 (b)), which hurts long-range modeling. (2) Region-specific global SA. Stripformer [52] explores horizontal and vertical intra-strip and inter-strip SA (Spa-SS represents **S**patial domain-**S**trip **S**patial-wise SA) (see Fig. 1 (c)), which relies on a strong assumption that image blur is usually regionally directional. (3) Coarse-grained global SA. Restormer [62] captures long-range interactions via Global Channel-wise SA (Spa-GC represents **S**patial domain-**G**lobal **C**hannel-wise SA) (see Fig. 1 (d)). Though Spa-GC can be learned, it inevitably focuses more on extracting low-frequency components of the image due to two reasons: (i) the energy of the image mainly lies in low-frequency, and (ii) when learned together, the high-frequency part is usually more

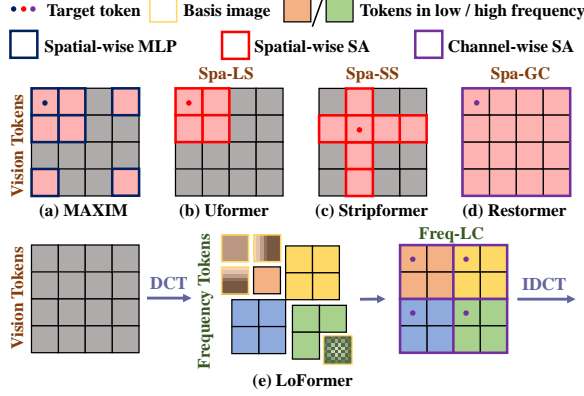


Figure 1: Different architectures of global feature learning. (a) MLP method in MAXIM [53]; (b) Window Self-Attention in Uformer [55]; (c) Strip Self-Attention in Stripformer [52]; (d) Global Channel Self-Attention in Restormer [62]; (e) Local Frequency Self-Attention in LoFormer. The vision tokens in spatial domain are converted to the DCT coefficients (frequency tokens) of different DCT basis images.

difficult to be processed than the lower-frequency part in practice [57]. Low-frequency part exhibits the coarse-grained level information, *e.g.*, the basic object structure, while the high-frequency part reflects fine-grained level information, *e.g.*, the texture details [59]. As is shown in Fig. 3, the motion blur kernel would effect both high- and low-frequency of the sharp image. Thus, coarse global SA like Spa-GC suffers from fine-grained correlation deficiency.

To model long-range dependency without compromise of fine-grained details, we presents Local Frequency Transformer (LoFormer) for image deblurring. Concretely, we propose **Frequency domain-Local Channel-wise SA (Freq-LC)** shown in Fig. 1 (e). First, we transform features into the frequency domain via Discrete Cosine Transform (DCT). DCT represents original features as the coefficients of different basis images. As shown in Fig. 1 (e), The basis images can be arranged in a rectangular grid, with lower frequency components in the top-left corner and higher frequency components towards the bottom-right. The top-left basis image represents the average intensity of the entire image, while the remaining basis images capture increasingly finer details and textures. The token at any frequency has global information. To allow equivalent learning opportunities for coarse-grained structures and fine-grained details, we design a window-based frequency feature extraction paradigm, *i.e.*, splitting frequency tokens into non-overlapping windows. The window on top left consists of tokens with coarse-grained structures (coarse tokens) and the one on bottom right consists of tokens with fine-grained details (fine tokens). Then, SAs are applied within local windows separately, capable of capturing cross-covariance within low- to high-frequency windows in parallel.

We further propose an intra-window MLP Gating (MGate) on the frequency axis complementary to Freq-LC, which performs a gating operation on the feature learned via SA. It's worth mentioning that

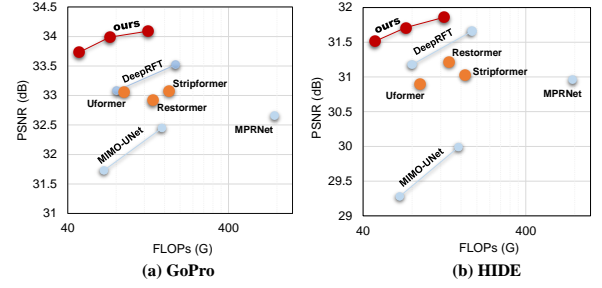


Figure 2: PSNR vs. FLOPs on the GoPro and HIDE datasets. Our method performs much better than other methods, especially Transformer based methods highlighted in orange.

the gating operation enhances the model capability of global information learning. We term our Freq-LC and intra-window MGate followed by a feed-forward network as **Local Frequency Transformer (LoFT)** block, which is the basic building block of LoFormer.

The main contributions can be summarized as follows:

- We propose simple yet effective Freq-LC to model long-range dependency without compromise of fine-grained details and introduce MGate which performs a gating operation and learns global features complementary to Freq-LC for better global information learning.
- We prove that Spa-GC equals to Freq-GC where coarse information dominates the calculation and verify that our Freq-LC has stronger capability in exploring divergent properties in frequency than Spa-GC.
- Extensive experiments show LoFormer achieves state-of-the-art results on image deblurring task, *e.g.*, 34.09 dB in PSNR for GoPro dataset. The PSNR (dB) vs. FLOPs (G) compared with state-of-the-arts are shown in Fig. 2.

2 Related Works

2.1 Deep Image Deblurring

Based on paired blurry-sharp image datasets, many methods [4, 5, 8, 16, 21, 24–26, 29, 34, 35, 37, 51, 53, 56, 63–65] adopt an end-to-end strategy to train a deep neural network for image deblurring task. To achieve better performance, most of the improvements revolve around the network structure or the specific components. For example, MPRNet [63] proposes a multi-stage architecture, which learns restoration functions progressively. MIMO-UNet [8] presents a multi-scale-input multi-scale-output UNet architecture to ease the difficulty of training. NAFNet [4] builds a network without activation and uses LayerNorm [1] (LN) to stabilize the training process with a high initial learning rate. Other methods such as Whang [56] introduces diffusion-based method for deblurring.

2.2 Low-level Vision Transformers

Transformer [54] was first proposed for natural language processing, and it has been widely used for various vision and multimodal tasks [2, 6, 14, 19, 20, 30, 44, 45, 48, 49, 61]. Recently, several Transformer models are explored for low-level vision tasks, such as image denoising [3, 55, 62], deblurring [52, 55, 62], deraining [3, 55, 62],



Figure 3: The visualization of various generated kernels and their impact on the sharpness of images within both the spatial and frequency domains. Specifically, the first row of the visualization pertains to the degraded image, while the second row illustrates the generated kernel. Furthermore, the odd columns represent the spatial domain, while the even columns depict the frequency domain.

and super-resolution [28]. Like model from ViT [14], IPT [3] applies a pre-trained Transformer model based on ImageNet [11] dataset for various image restoration tasks. SwinIR [28] and Uformer [55] apply window-based SA [31] to capture long-range dependencies. Stripformer [52] decomposes the spatial-wise global SA into horizontal and vertical SA. Restormer [62] models global context by applying SA across channels with linear complexity rather than spatial. Though extensive efforts have been made to capture long-range dependencies, either conducting pixel-wise SA on a local window or learning global context in a sparse manner, they neglect an important fact that independent components within an image/feature should not be blindly modeled altogether via SA operations. We propose to decompose features into independent components, *i.e.*, frequency tokens, by projecting them onto orthogonal bases via DCT and conduct global context learning within each partitioned frequency window.

2.3 Frequency Domain Applications

A growing literature corpus has proposed methods extracting information from the frequency domain to fulfill various tasks [13, 17, 18, 22, 33, 36, 42, 47, 58, 60, 67, 68]. FcaNet [39] generalizes the channel attention in the frequency domain for image classification; GFNet [40] learns long-term spatial dependencies in the frequency domain. LaMa [50] uses the structure of fast fourier convolution [7] as the building block to image inpainting. DeepRFT [35] introduces a simple Res-FFT-ReLU block into deep networks for image deblurring. FAD [57] divides the input feature into multiple components based on a frequency-domain predictor for image super-resolution. MBCNN [66] proposes a multi-block-size learnable bandpass filters to learn the frequency priors of moire patterns. CRAFT [27] enhances high-frequency feature by CNN and learns global information by Transformer. Inspired by the success of frequency domain, we propose an LoFT block which enables (1) independent components decomposition via DCT, and (2) globally independent context learning in a frequency window.

3 Method

3.1 Main Backbone

An overview of LoFormer architecture is shown in Fig. 4. LoFormer employs a UNet [43] architecture proposed by Restormer [62] as the backbone. In Restormer, each stage of encoder-decoder contains multiple Transformer blocks. We design a **Local Frequency Transformer** (LoFT) block as our building block. As illustrated in Table 1, we put more building blocks to lower stages for efficiency, *i.e.*, from stage-1 to stage-4, the number of LoFT blocks are [2, 4, 6, 14] (LoFormer-S), [2, 4, 12, 18] (LoFormer-B and LoFormer-L) and number of attention heads are [1, 2, 4, 8]. The refinement contains two LoFT blocks.

3.2 Local Frequency Transformer Block

LoFT block consists of a proposed Local Frequency Network (LoFN) and a Feed-Forward Network (FFN). As shown in Fig. 4, the LoFN consists of (i) LayerNorm after DCT (DCT-LN), (ii) Frequency domain-Local Channel-wise SA (Freq-LC), (iii) intra-window MLP Gating in the frequency domain (MGate). For FFN, we adopt the Gated-Dconv Feed-forward Network (GDFN) in Restormer [62].

First, we apply DCT transform on feature map \mathbf{X}_{in}^c of c th channel via:

$$\mathbf{Z}_{\text{dct}}^{h,w,c} = \sum_{u=0}^{H-1} \sum_{v=0}^{W-1} \mathbf{X}_{\text{in}}^{u,v,c} \cdot \mathbf{B}_{h,w}^{u,v}, \quad (1)$$

where $\mathbf{Z}_{\text{dct}}^c \in \mathbb{R}^{H \times W}$ is the DCT frequency tokens, H and W are height and width of \mathbf{X}_{in}^c , respectively. $\mathbf{B}_{h,w}^{u,v} \in \mathbb{R}^{H \times W}$ is the basis image of the corresponding DCT coefficient located in $\mathbf{Z}_{\text{dct}}^{h,w,c}$, and there are $H \times W$ basis images for \mathbf{X}_{in}^c . Given indices h, w :

$$\mathbf{B}_{h,w}^{u,v} = F(u)F(v) \cos\left(\frac{\pi h}{H}\left(u + \frac{1}{2}\right)\right) \cos\left(\frac{\pi w}{W}\left(v + \frac{1}{2}\right)\right) \quad (2)$$

s.t. $u \in \{0, 1, \dots, H-1\}, v \in \{0, 1, \dots, W-1\}$,

$$\text{where } F(u) = \begin{cases} \frac{1}{\sqrt{2}} & u = 0 \\ 1 & u > 0 \end{cases}, F(v) = \begin{cases} \frac{1}{\sqrt{2}} & v = 0 \\ 1 & v > 0 \end{cases}.$$

Next, we describe DCT-LN, Freq-LC and MGate, respectively.

DCT-LN. LN [1] has been widely adopted in computer vision tasks due to its ability of stabilizing the training process [4]. Given

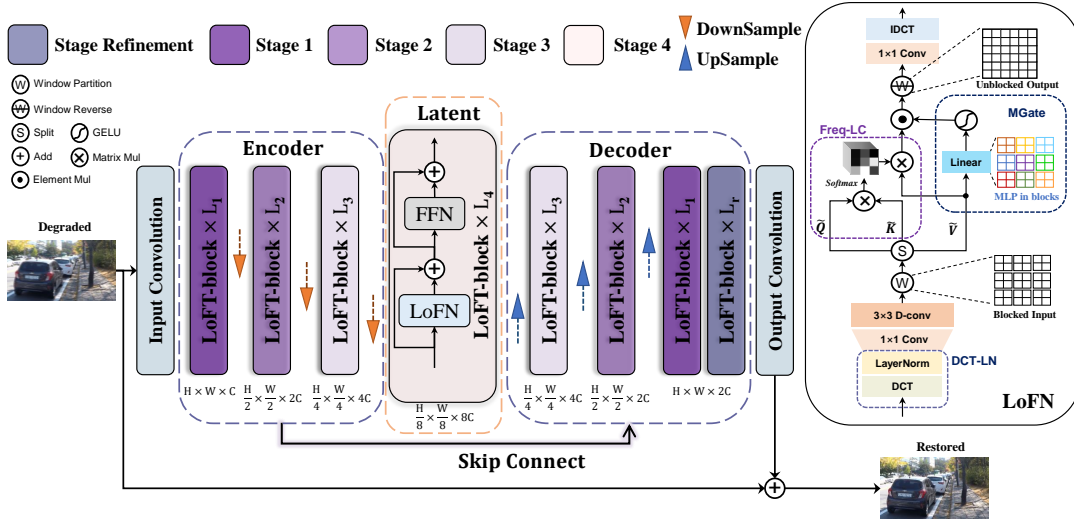


Figure 4: Architecture of LoFormer. The main backbone of LoFormer is an UNet [43] model built in Restormer [62]. The basic building block of LoFormer is Local Frequency Transformer block (LoFT-block), which consists of a Local Frequency Network (LoFN) module and an Feed-Forward Network (FFN) module. The core components of LoFN are DCT-LN, Freq-LC and MGate on frequency windows that perform global context aggregation.

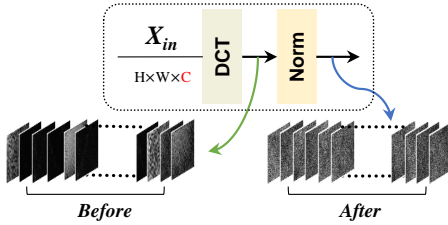


Figure 5: LayerNorm after DCT.

the feature in spatial domain $\mathbf{X}_{in} \in \mathbb{R}^{H \times W \times C}$, as shown in Fig. 5, we first apply DCT to obtain the frequency tokens $\mathbf{Z}_{dct} = \text{DCT}(\mathbf{X}_{in}) \in \mathbb{R}^{H \times W \times C}$. Then, the LN after DCT can be defined as:

$$\mathbf{Z}_{norm} = \frac{\mathbf{Z}_{dct} - \bar{\mathbf{Z}}_{dct}}{\hat{\mathbf{Z}}_{dct}} \times \gamma + \beta, \quad (3)$$

where $\bar{\mathbf{Z}}_{dct} = \frac{1}{C} \sum_{c=1}^C \mathbf{Z}_{dct}^c$, and $\hat{\mathbf{Z}}_{dct} = \sqrt{\frac{1}{C} \sum_{c=1}^C (\mathbf{Z}_{dct}^c - \bar{\mathbf{Z}}_{dct})^2 + \epsilon}$ is the standard deviation of \mathbf{Z}_{dct} along the channel dimension. γ and β are learnable parameters, and $\epsilon = 10^{-5}$. After DCT, The distribution of frequency tokens varies greatly. Large amount of information stored in low frequency, and less information stored in the rest frequency. Thus, we adopt LN to force frequency tokens to be distributed equally, which is important to stabilize the training process. It is worth mentioning that applying LN before DCT would be equivalent of applying convolution in frequency domain (resulting from a simple calculation), which do not help in balancing the distribution of frequency tokens.

Freq-LC. Given the feature $\mathbf{X}_{norm} \in \mathbb{R}^{H \times W \times C}$, we first apply 1×1 convolutions to obtain frequency-wise cross-channel context, and

Table 1: Hyper-parameters with LoFormer. $[L_1 \sim L_4]$ and L_r denote the number of LoFT block in stage-1,2,3,4 and refinement. C is the feature dimension. PSNR(dB) is calculated on GoPro [37] dataset. FLOPs (G) are calculated on an input RGB image of size 256×256 . Params are calculated in (M).

Model	$[L_1 \sim L_4]$	L_r	C	PSNR	Params	FLOPs
Restormer	[4,6,6,8]	4	48	32.92	26.12	135
LoFormer-S	[2,4,6,14]	2	32	33.73	16.38	47
LoFormer-B	[2,4,12,18]	2	36	33.99	27.93	73
LoFormer-L	[2,4,12,18]	2	48	34.09	49.03	126

Table 2: Explanation of some symbols.

Sym	Explanation	Sym	Explanation
H	: Height	N	= HW: Resolution of tensor
W	: Width	\hat{C}	= C/r: Channel for SA
C	: Channel	n	= b^2 : Resolution of window
b	: Window	m	= N/n: Numbers of windows
r	: SA heads		

then 3×3 depth-wise convolutions are employed to gather channel-wise frequency local context. Through this way, we acquire $\tilde{\mathbf{Q}}, \tilde{\mathbf{K}}$ and $\tilde{\mathbf{V}} \in \mathbb{R}^{r \times \hat{C} \times N}$ representing queries, keys, and values, where N, \hat{C} and r are indicated in Table 2. Noted that we use different channels to represent multi-head. Then we design a window partition method and split $\tilde{\mathbf{Q}}, \tilde{\mathbf{K}}$ and $\tilde{\mathbf{V}}$ into non-overlapping windows with the window size of $b \times b$, acquiring $\tilde{\mathbf{Q}}, \tilde{\mathbf{K}}$, and $\tilde{\mathbf{V}} \in \mathbb{R}^{m \times r \times \hat{C} \times n}$, where m and n are indicated in Table 2. As shown in Fig. 4, we perform Local SA on the channel axis of $\tilde{\mathbf{Q}}, \tilde{\mathbf{K}}$, and $\tilde{\mathbf{V}}$. From each window i , features

$\tilde{\mathbf{Q}}_i, \tilde{\mathbf{K}}_i$, and $\tilde{\mathbf{V}}_i \in \mathbb{R}^{\hat{C} \times n}$ can be obtained via flattening and transposing operations. Next, we perform SA to generate a transposed-attention map $\tilde{\mathbf{A}}_i \in \mathbb{R}^{\hat{C} \times \hat{C}}$ for window i . The process can be defined as $\tilde{\mathbf{A}}_i = \text{Softmax}(\tilde{\mathbf{Q}}_i \cdot \tilde{\mathbf{K}}_i^\top / \alpha)$ and $\text{Attention}(\tilde{\mathbf{Q}}_i, \tilde{\mathbf{K}}_i, \tilde{\mathbf{V}}_i) = \tilde{\mathbf{A}}_i \cdot \tilde{\mathbf{V}}_i$.

The transposed-attention map for all windows can be written as $\tilde{\mathbf{A}} = \{\tilde{\mathbf{A}}_1, \tilde{\mathbf{A}}_2, \dots, \tilde{\mathbf{A}}_m\}$, where $\tilde{\mathbf{A}} \in \mathbb{R}^{m \times r \times \hat{C} \times \hat{C}}$, and α is a trainable scaling parameter.

MGate. To emphasize on the frequency, and control which complementary features should flow forward combined with Freq-LC, we apply MGate through intra-window MLP shown in Fig. 4 while sharing parameters on the other axes:

$$\text{MGate}(\tilde{\mathbf{V}}_i) = \sigma(\text{Linear}(\tilde{\mathbf{V}}_i)), \quad (4)$$

where σ indicates GELU operation. The intra-window MGate operation achieves local frequency mixing via aggregating cross-frequency context. Due to the global properties of each token in the frequency domain, it enhances the global information learned by Freq-LC from a different point of view. By combining Freq-LC and MGate branches together via element-wise multiplication, LoFT block can achieve superior performance to other counterparts.

After combining the output from Freq-LC and MGate by dot product, we perform window reverse to transpose the feature back to size $H \times W \times C$, and apply 1×1 convolutions to fuse cross-channel context indicated as \mathbf{Z}_{axis} . Correspondingly, we perform inverse DCT transform on feature map \mathbf{Z}_{axis} , whose feature on the c th channel is $\mathbf{Z}_{\text{axis}}^c$:

$$\mathbf{X}_{\text{idct}}^c = \sum_{h=0}^{H-1} \sum_{w=0}^{W-1} \mathbf{Z}_{\text{axis}}^{h,w,c} \cdot \mathbf{B}_{h,w}, \quad (5)$$

where $\mathbf{B}_{h,w} \in \mathbb{R}^{H \times W}$ is the basis image for the corresponding DCT coefficient, $\mathbf{X}_{\text{idct}}^c \in \mathbb{R}^{H \times W}$ is the feature on the c th channel of \mathbf{X}_{idct} .

Complexity analysis. As shown in Table 3, our Freq-LC shares the same computation complexity of Convolution and Attention compared with Spa-GC in Restormer [62]. Furthermore, the computational complexity of DCT required by the proposed approach only increases a manageable $O(N \log_2(N))$ while providing a significant improvement in performance.

4 Understanding SA in the Frequency Domain

4.1 Spa-GC is equivalent to Freq-GC

For better reading, Table 3 lists different SA methods. To understand the physical meaning of matrix multiplication in the frequency domain, we explore the relationship between Spa-GC and Freq-GC. We have the proposition below:

PROPOSITION 1. *Spa-GC: $\mathbf{O} = \text{Attention}(\mathbf{Q}, \mathbf{K}, \mathbf{V})$ and Freq-GC: $\hat{\mathbf{O}}_f = \text{IDCT}(\hat{\mathbf{O}}) = \text{IDCT}(\text{Attention}(\hat{\mathbf{Q}}, \hat{\mathbf{K}}, \hat{\mathbf{V}}))$ are identical, without considering depth-wise convolutions and DCT-LN, where queries, keys, and values are $\mathbf{Q}, \mathbf{K}, \mathbf{V}$ in the spatial domain, and $\hat{\mathbf{Q}}, \hat{\mathbf{K}}, \hat{\mathbf{V}}$ in the frequency domain.*

Proof for Proposition 1. For simplicity, we elaborate the deviation in 2D matrices instead of 3D tensors, e.g., simplifying the size of the features $\hat{C} \times H \times W$ to $\hat{C} \times N$, where $N = HW$, shown below. The

Table 3: Comparison of different SAs. Spa, Freq, LS, GC, and LC mean Spatial, Frequency, Local Spatial-wise SA, Global Channel-wise SA, and Local Channel-wise SA, respectively. Spa Filter-GC means performing pass filters of different frequencies on the spatial feature, and then aggregating all global information. Symbols in computation complexity are indicated in Table 2. FLOPs (M) are calculated with $H = W = 256, C = 32, b = 8, r = 1$.

SA	Model	Computation Complexity	FLOPs
Spa-LS	Uformer	$2NCn$	268
Spa-GC	Restormer	$2NC\hat{C}$	134
Freq-GC	-	$2NC(\hat{C} + \log_2(N))$	201
Spa Filter-GC	-	$2NC(N\hat{C} + \log_2(N))$	$\gg 10^3$
Freq-LC	LoFormer	$2NC(\hat{C} + \log_2(N))$	201

output features represented in the spatial domain after performing global SA on queries, keys, and values on the spatial ($\mathbf{Q}, \mathbf{K}, \mathbf{V} \in \mathbb{R}^{\hat{C} \times N}$) and frequency ($\hat{\mathbf{Q}}, \hat{\mathbf{K}}, \hat{\mathbf{V}} \in \mathbb{R}^{\hat{C} \times N}$) domains can be obtained via:

$$\mathbf{O} = \text{Softmax}(\mathbf{Q} \cdot \mathbf{K}^\top) \cdot \mathbf{V} \quad (6)$$

$$\begin{aligned} \hat{\mathbf{O}}_f &= \text{IDCT}(\hat{\mathbf{O}}) = \text{Softmax}(\hat{\mathbf{Q}} \cdot \hat{\mathbf{K}}^\top) \cdot \hat{\mathbf{V}} \cdot \mathbf{D}^\top \\ &= \text{Softmax}(\mathbf{Q} \cdot \mathbf{D} \cdot \mathbf{D}^\top \cdot \mathbf{K}^\top) \cdot \mathbf{V} \cdot \mathbf{D} \cdot \mathbf{D}^\top \\ &= \text{Softmax}(\mathbf{Q} \cdot \mathbf{K}^\top) \cdot \mathbf{V} = \mathbf{O}, \end{aligned} \quad (7)$$

where $\mathbf{D} \in \mathbb{R}^{N \times N}$ is the matrix representation of DCT coefficients, and $\hat{\mathbf{O}}_f$ means the SA which is calculated in the frequency domain and then transformed back to the spatial domain via inverse DCT. Since \mathbf{D} is orthogonal matrix, $\mathbf{D} \cdot \mathbf{D}^\top$ is unit matrix.

4.2 Analysis of Freq-LC from Spatial Perspective

We argue that our Freq-LC learns both coarse- and fine-grained global features, and explores different properties in representation. In this section, we analyze Freq-LC in the frequency domain from a new perspective.

As illustrated in Eq. 5, for an image with the size of $H \times W$, it can be represented as the sum of a series of basis images $\mathbf{B}_{h,w} \in \mathbb{R}^{H \times W}$ with the corresponding DCT coefficient, where $h \in \{0, \dots, H-1\}$, $w \in \{0, \dots, W-1\}$. We have the following proposition holds:

PROPOSITION 2. *Our Freq-LC can be seen as performing pass filters on a spatial feature, by representing the frequency tokens within a specific window as the summation of their corresponding basis images in the spatial domain. Compared to Freq-LC which applies Local Channel-wise SA on specific frequency tokens, realizing Freq-LC in the spatial domain would result in a significant increase in both memory and computation complexity.*

Proof for Proposition 2. We design a window partition method (window size = $b \times b$) and obtain $\tilde{\mathbf{Q}}, \tilde{\mathbf{K}}$ and $\tilde{\mathbf{V}} \in \mathbb{R}^{m \times \hat{C} \times n}$, where $n = b^2$ and $m = N/n$ after the window partition on \mathbf{Q}, \mathbf{K} and \mathbf{V} , respectively. From each window i , features $\tilde{\mathbf{Q}}_i, \tilde{\mathbf{K}}_i, \tilde{\mathbf{V}}_i \in \mathbb{R}^{\hat{C} \times n}$ can

Table 4: Summary of five public datasets.

Task	Dataset	Train	Val	Test	Types
Motion Deblur	GoPro [37]	2,103	-	1,111	synthetic
	HIDE [46]	-	-	2,025	synthetic
	RealBlur-R [41]	3,758	-	980	real-world
	RealBlur-J [41]	3,758	-	980	real-world
	REDS [38]	24,000	3,000	300	synthetic

be obtained via flattening and transposing operations. Let's assume padding $\tilde{\mathbf{Q}}_i$, $\tilde{\mathbf{K}}_i$, and $\tilde{\mathbf{V}}_i$ to size $\hat{C} \times N$ with zeros, obtaining $\tilde{\mathbf{Q}}_i$, $\tilde{\mathbf{K}}_i$ and $\tilde{\mathbf{V}}_i$. $\tilde{\mathbf{Q}}_i$, $\tilde{\mathbf{K}}_i$ and $\tilde{\mathbf{V}}_i$ can be regarded as the frequency spectrum after applying corresponding pass filters on features in the spatial domain. The output frequency features after applying SA for the i th window on $\tilde{\mathbf{Q}}_i$, $\tilde{\mathbf{K}}_i$ and $\tilde{\mathbf{V}}_i$ before padding and on $\tilde{\mathbf{Q}}_i$, $\tilde{\mathbf{K}}_i$ and $\tilde{\mathbf{V}}_i$ after padding can be calculated as:

$$\tilde{\mathbf{O}}_i = \text{Softmax}(\tilde{\mathbf{Q}}_i \cdot \tilde{\mathbf{K}}_i^\top) \cdot \tilde{\mathbf{V}}_i \quad (8)$$

$$\tilde{\mathbf{O}}_i = \text{Softmax}(\tilde{\mathbf{Q}}_i \cdot \tilde{\mathbf{K}}_i^\top) \cdot \tilde{\mathbf{V}}_i, \quad (9)$$

Noted that $\tilde{\mathbf{Q}}_i \cdot \tilde{\mathbf{K}}_i^\top = \tilde{\mathbf{Q}}_i \cdot \tilde{\mathbf{K}}_i^\top$. Thus, after window reverse (*wr*) operation, the total output of local SA is aggregated by:

$$\begin{aligned} \tilde{\mathbf{O}} &= \sum_{i=1}^m \tilde{\mathbf{O}}_i = \sum_{i=1}^m \text{Softmax}(\tilde{\mathbf{Q}}_i \cdot \tilde{\mathbf{K}}_i^\top) \cdot \tilde{\mathbf{V}}_i \\ &= \sum_{i=1}^m \text{Softmax}(\tilde{\mathbf{Q}}_i \cdot \tilde{\mathbf{K}}_i^\top) \cdot \tilde{\mathbf{V}}_i \end{aligned} \quad (10)$$

$$\begin{aligned} \tilde{\mathbf{O}}_w &= wr(\tilde{\mathbf{O}}_i) = wr(\text{Softmax}(\tilde{\mathbf{Q}}_i \cdot \tilde{\mathbf{K}}_i^\top) \cdot \tilde{\mathbf{V}}_i) \\ &= \sum_{i=1}^m \text{Softmax}(\tilde{\mathbf{Q}}_i \cdot \tilde{\mathbf{K}}_i^\top) \cdot \tilde{\mathbf{V}}_i = \tilde{\mathbf{O}}, \end{aligned} \quad (11)$$

where $\tilde{\mathbf{O}}_w$ means the SA calculated in local windows and then window reversing to obtain the total output.

Although the above two operations lead to identical results in terms of accuracy, they have different efficiency. We summarize the computation complexity of different SAs in Table 3, including SAs used in popular methods such as Uformer and Restormer. Our Freq-LC (see Freq-LC (LoFormer) in Table 3) is much more efficient compared with aggregating global SAs in spatial (Spa Filter-GC).

5 Experiment

5.1 Experimental Setup

Dataset. We evaluate our method on the five datasets summarized in Table 4. Since existing methods adopt different experimental settings, we summarize them and report three groups of results:

- \mathcal{A} . train on GoPro, and test on GoPro / HIDE respectively;
- \mathcal{B} . train and test on RealBlur-J / RealBlur-R respectively;
- \mathcal{C} . train and test on REDS dataset (follow HINet [5]).

Implementation Details. We adopt the training strategy used in Restormer [62] unless otherwise specified. *I.e.*, the network training

Table 5: Comparison on GoPro [37], HIDE [46] datasets for setting \mathcal{A} . Transformer-based methods are highlighted.

Method	GoPro		HIDE		Params FLOPs	
	PSNR	SSIM	PSNR	SSIM	M	G
MPRNet [63]	32.66	0.959	30.96	0.939	20.1	588
MIMO-UNet+ [8]	32.45	0.957	29.99	0.930	16.1	154
EFEP [13]	33.27	0.974	31.57	0.951	23.9	113
FocalNet [10]	33.10	0.962	-	-	15.9	143
SFNet [10]	33.27	0.963	31.10	0.941	13.3	125
DeepRFT+ [35]	33.52	0.965	31.66	0.946	23.0	187
UFPNet [15]	34.06	0.968	31.74	0.947	80.3	243
Uformer [55]	33.06	0.967	30.90	0.953	50.9	90
Restormer [62]	32.92	0.961	31.22	0.942	26.1	135
Stripformer [52]	33.08	0.962	31.03	0.940	20.0	170
MRLPFNet [12]	34.01	0.968	31.63	0.947	20.6	129
LoFormer-S	33.73	0.966	31.51	0.946	16.4	47
LoFormer-B	33.99	0.968	31.71	0.948	27.9	73
LoFormer-L	34.09	0.969	31.86	0.949	49.0	126

hyperparameters (and the default values we use) are learning strategy (progressive learning), data augmentation (horizontal and vertical flips), training iterations (600k), optimizer AdamW ($\beta_1 = 0.9$, $\beta_2 = 0.999$, weight decay 1×10^{-4}), initial learning rate (3×10^{-4}). The learning rate is steadily decreased to 1×10^{-6} using the cosine annealing strategy [32]. For LoFormer-S and LoFormer-B, we start training with patch size 128×128 and batch size 64. The patch size and the batch size pairs are updated to [(160, 40), (192, 32), (256, 16), (320, 8), (384, 8)] at iterations [184K, 312K, 408, 480K, 552K]. Due to statistics distribution shifts between training and testing [9], we utilize a step of 352 to perform 384×384 size sliding window with an overlap-size of 32 for testing. We set $b = 8$ for LoFormer-S and LoFormer-B. In the selection of the loss function, two kinds of loss functions are utilized: (1) L1 loss: $\mathcal{L}_1 = \|\hat{\mathbf{S}} - \mathbf{S}\|_1$, and (2) Frequency Reconstruction (FR) loss [8, 35, 53]: $\mathcal{L}_{fr} = \|\mathcal{F}(\hat{\mathbf{S}}) - \mathcal{F}(\mathbf{S})\|_1$. Where $\hat{\mathbf{S}}$, \mathbf{S} and $\mathcal{F}(\cdot)$ represent the predicted sharp image, the groundtruth sharp image and 2D Fast Fourier Transform, respectively. For LoFormer, the loss function $\mathcal{L} = \mathcal{L}_1 + 0.01\mathcal{L}_{fr}$.

Evaluation metric. Performances in terms of PSNR and SSIM over all testing sets, as well as the number of parameters and FLOPs are calculated using official algorithms.

5.2 Main Results

Setting \mathcal{A} . For setting \mathcal{A} , we train our model on 2,103 image pairs from GoPro [37], and compare them with several SOTA methods through the test set of GoPro [37] and HIDE [46]. As shown in Table 5 and Fig. 6, LoFormer outperforms the other CNN-based, Transformer-based and MLP-based methods in both PSNR and SSIM on the GoPro test set. Under the same training strategy, our LoFormer-L achieves 1.17 dB gain over Restormer [62] with similar FLOPs (126G vs. 135G). Besides, LoFormer-L obtains robust results on other datasets. For HIDE test set, LoFormer-L achieves



Figure 6: Examples on the GoPro test dataset. LoFormer produces better result.

Table 6: Comparison on RealBlur [41] dataset for setting \mathcal{B} .

Method	RealBlur-R		RealBlur-J		Params FLOPs	
	PSNR	SSIM	PSNR	SSIM	M	G
SRN [51]	38.65	0.965	31.38	0.909	-	-
MPRNet [63]	39.31	0.972	31.76	0.922	20.1	777
MAXIM [53]	39.45	0.962	32.84	0.935	22.2	339
DeepRFT+ [35]	40.01	0.973	32.63	0.933	23.0	187
Stripformer [52]	39.84	0.974	32.48	0.929	20.0	170
FFTformer [23]	40.11	0.975	32.62	0.933	16.6	132
LoFormer-B	40.23	0.974	32.90	0.933	27.9	73

Table 7: Comparison on the REDS-val-300 from REDS [38] dataset of NTIRE 2021 Image Deblurring Challenge Track 2 JPEG artifacts for setting \mathcal{C} .

Model	PSNR	SSIM	FLOPs	Params
MPRNet	28.79	0.811	777	20.1
HINet	28.83	0.862	171	88.7
MAXIM	28.93	0.865	339	22.2
NAFNet64	29.09	0.867	64	65.0
LoFormer-B	29.20	0.869	73	27.9

31.86dB, 0.64dB higher than Restormer. Note that as mentioned in the introduction, Spa-LS in Uformer hurts long-range modeling, Spa-SS in Stripformer relies on a strong assumption, and Spa-GC in Restormer suffers from fine-grained correlation deficiency, while our Freq-LC consists of simple yet effective operations to model long-range dependency without losing fine-grained details.

Setting \mathcal{B} . As can be seen in Table 6, LoFormer-B achieves 32.90dB on RealBlur-J test set, 0.42dB higher than Stripformer [52] with fewer FLOPs (73G vs. 170G). For RealBlur-R, LoFormer-B also gets a better outcome (40.23dB) than Stripformer (39.84dB).

Table 8: Ablation studies. LN-DCT: LayerNorm followed by DCT. DC: Dilated Channel-wise SA with a dilated stride of $[H/b, W/b]$. CGate: applying Linear on the channel axis.

Attention	LN-DCT	DCT-LN	MGate	PSNR	FLOPs
Spa-GC	×	×	×	32.74	43.33
Freq-GC	✓	×	×	32.68	44.46
	×	✓	×	32.84	44.46
Freq-DC	✓	×	×	32.75	44.46
	×	✓	×	32.90	44.46
Freq-LS	✓	×	×	32.95	45.90
	×	✓	×	33.15	45.90
Freq-LC	✓	×	×	32.91	44.46
	✓	×	✓	32.94	46.97
	×	✓	×	33.17	44.46
	×	✓	CGate	32.97	47.95
	×	✓	✓	33.23	46.97
LoFormer-B	×	✓	×	33.54	69.68
	×	✓	✓	33.99	73.04

Setting \mathcal{C} . Moreover, LoFormer-B achieves a competitive result with other methods for REDS [38] dataset shown Table 7, e.g., 0.27dB better than MAXIM. In brief, the quantitative experimental results indicate that our LoFormer has a good ability to handle motion deblurring tasks under different conditions.

5.3 Analysis and Discussion

Extensive ablation studies are conducted to verify the effectiveness of LoFT block *w.r.t.* different components. The models are trained on GoPro with progressive learning strategy for 300K iterations. The training starts with patch size 128×128 and batch size 32, which shares the same hyper-parameters of the model design with LoFormer-S.

5.4 Effectiveness of DCT-LN

We propose to conduct Layer Normalization (LN) on the frequency-transformed matrix \mathbf{X}_{det} rather than the input matrix \mathbf{X}_{in} , aiming to ensure an equitable distribution of frequency tokens, thereby

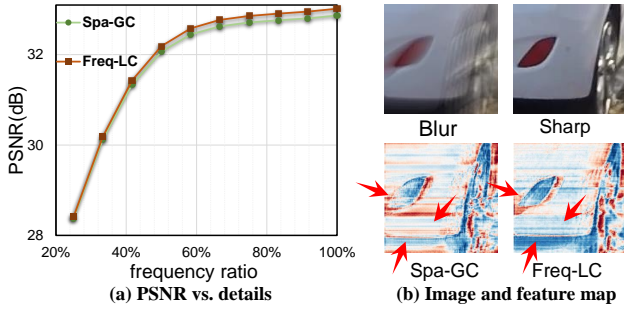


Figure 7: (a) PSNR vs. details on GoPro. The higher ratio means in testing, more high-frequency information (details) of the restored images is included when calculating PSNR. Freq-LC performs better than Spa-GC on details. (b) Feature maps of Spa-GC and Freq-LC. Freq-LC gets better details.

promoting training stability. As demonstrated in Table 8, the utilization of DCT-LN alongside Freq-LC results in superior performance, yielding a 0.26 dB improvement compared to employing LN-DCT (32.91 dB). Similarly, for Freq-GC, employing DCT-LN contributes to a gain of 0.16 dB.

5.5 Effectiveness of Local Attention

In the frequency domain, we can easily acquire global information of the input feature \mathbf{X}_{in} within a local window of \mathbf{X}_{dct} . Compared with Freq-GC (32.68dB) in Table 8, Freq-LC acquires a gain of 0.23 dB in PSNR (32.91dB). Fig. 7 (a) shows masking different detail ratios of restored images when computing PSNRs. Freq-LC is more capable of capturing **high-frequency details**, which are suppressed by structure features in popular Spa-GC (see Fig. 8(a)). In addition, Fig. 7 (b) further indicates that Freq-LC acquires better feature details than Spa-GC for deblurring. Freq-LC performs similarly to Spa-GC in low-freq, but it achieves better results when involving more high-freq, showing Freq-LC restores details better than Spa-GC. Moreover, we design a Dilated Channel-wise SA in the frequency domain (Freq-DC) to further verify the effectiveness of learning coarse-and-fine information separately in SA. Even applying DCT-LN to make frequency tokens to be distributed equally, Freq-DC (32.90dB) performs 0.27dB worse than Freq-LC (33.17dB).

5.6 Effectiveness of MGate

Table 8 shows that MGate boosts the effectiveness of Freq-LC in linear time, and helps Freq-LC filter out the invalid information, which let LoFormer-B develop deeper (33.99dB w/ MGate vs. 33.54dB w/o MGate). Additionally, we perform MLP on the channel axis of \mathbf{X}_{dct} , named as CGate. The performance drops compared with MGate (32.97dB vs. 33.23dB in Table 8), showing the complementary feature provided via MGate operation.

5.7 Discussion

Spatial or Channel. As delineated in Table 8, the efficacy of Freq-LS (33.15 dB, 45.90G) exhibits a comparative level to that of

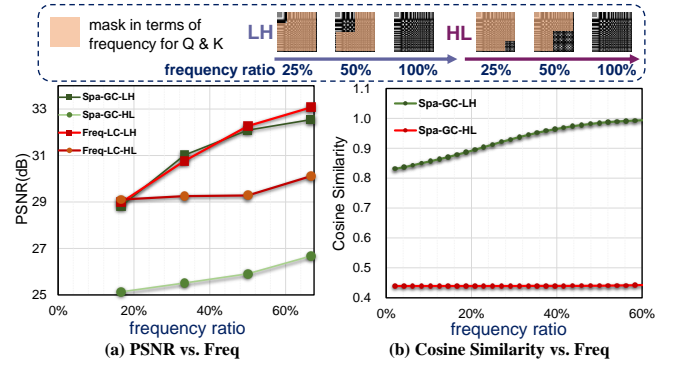


Figure 8: The analysis for Spa-GC and Freq-LC on GoPro. (a) PSNR vs. proportions of Low-frequency (LF) or High-frequency (HF); (b) The cosine similarity of Spa-GC between the source attention map through different ratios of LF/HF and the target attention map through all the information.

Freq-LC (33.17 dB, 44.46G), with the former incurring slightly elevated computational complexity. Consequently, we opt to integrate Freq-LC into the LoFormer architecture.

Superiority of Freq-LC. To demonstrate the superior ability of Freq-LC over Spa-GC in learning fine-grained high-frequency features, a comparison is made between the two methods by plotting PSNR curves against low-/high-frequency ratio on Fig. 8 (a). The purpose of this analysis is to highlight the advantage of Freq-LC in capturing subtle details that may be suppressed by structure features in Spa-GC. We test LoFormer framework with Freq-LC and Spa-GC, but with different selected frequency ratios. Our Freq-LC observes a performance boost at a faster rate (see Freq-LC-LF and Spa-GC-LF) when involving more and more high-frequency parts. Conversely, involving more low-frequency parts does not change the performance of Freq-LC dramatically like Spa-GC (see Freq-LC-HF and Spa-GC-HF), which proves that high-frequency information plays a more important role in Freq-LC than Spa-GC. Similarly, Fig. 8 (b) shows Spa-GC does not effectively learn high-frequency information, whose cosine similarity with the attention map of Spa-GC is small (see Spa-GC-HF). Besides, computing SA within different frequency windows helps to explore divergent properties in representation.

6 Conclusions

We introduce a novel approach termed Local Frequency Transformer (LoFormer) for image deblurring. In contrast to prior transformer methodologies that focus on either learning localized self-attention (SA) mechanisms or adopting coarse-grained global SA strategies to mitigate computational complexity, LoFormer offers a unique solution. It simultaneously captures both coarse- and fine-grained long-range dependencies by employing channel-wise self-attention within localized frequency token windows. Moreover, we incorporate MLP Gating to augment global learning capabilities and eliminate irrelevant features. Extensive experiments across five image deblurring datasets demonstrates the superior performance of our proposed LoFormer.

7 Acknowledgement

This work was supported by the National Natural Science Foundation of China (Grant No. 62101191, 61975056), Shanghai Natural Science Foundation (Grant No. 21ZR1420800), and the Science and Technology Commission of Shanghai Municipality (Grant No. 22S31905800, 22DZ2229004).

References

- [1] Lei Jimmy Ba, Jamie Ryan Kiros, and Geoffrey E. Hinton. 2016. Layer Normalization. *CoRR* abs/1607.06450 (2016).
- [2] Nicolas Carion, Francisco Massa, Gabriel Synnaeve, Nicolas Usunier, Alexander Kirillov, and Sergey Zagoruyko. 2020. End-to-End Object Detection with Transformers. In *Proc. ECCV*. 213–229.
- [3] Hanting Chen, Yunhe Wang, Tianyu Guo, Chang Xu, Yiping Deng, Zhenhua Liu, Siwei Ma, Chunjing Xu, Chao Xu, and Wen Gao. 2021. Pre-Trained Image Processing Transformer. In *Proc. CVPR*.
- [4] Liangyu Chen, Xiaojie Chu, Xiangyu Zhang, and Jian Sun. 2022. Simple Baselines for Image Restoration. In *Proc. ECCV*.
- [5] Liangyu Chen, Xin Lu, Jie Zhang, Xiaojie Chu, and Chengpeng Chen. 2021. HINet: Half Instance Normalization Network for Image Restoration. In *Proc. CVPR Workshop*.
- [6] Mark Chen, Alec Radford, Rewon Child, Jeffrey Wu, Heewoo Jun, David Luan, and Ilya Sutskever. 2020. Generative Pretraining From Pixels. In *Proc. ICML*. 1691–1703.
- [7] Lu Chi, Borui Jiang, and Yadong Mu. 2020. Fast Fourier Convolution. In *Proc. NeurIPS*, Hugo Larochelle, Marc'Aurelio Ranzato, Raia Hadsell, Maria-Florina Balcan, and Hsuan-Tien Lin (Eds.).
- [8] Sung-Jin Cho, Seo-Won Ji, Jun-Pyo Hong, Seung-Won Jung, and Sung-Jea Ko. 2021. Rethinking Coarse-to-Fine Approach in Single Image Deblurring. In *Proc. ICCV*.
- [9] Xiaojie Chu, Liangyu Chen, Chengpeng Chen, and Xin Lu. 2022. Improving Image Restoration by Revisiting Global Information Aggregation. In *Proc. ECCV*.
- [10] Yuning Cui, Wenqi Ren, Xiaochun Cao, and Alois Knoll. 2023. Focal Network for Image Restoration. In *Proc. ICCV*.
- [11] Jia Deng, Wei Dong, Richard Socher, Li-Jia Li, Kai Li, and Li Fei-Fei. 2009. ImageNet: A large-scale hierarchical image database. In *Proc. CVPR*.
- [12] Jiangxin Dong, Jinshan Pan, Zhongbao Yang, and Jinhui Tang. 2023. Multi-Scale Residual Low-Pass Filter Network for Image Deblurring. In *Proc. ICCV*.
- [13] Shuting Dong, Zhe Wu, Feng Lu, and Chun Yuan. 2023. Enhanced Image Deblurring: An Efficient Frequency Exploitation and Preservation Network. In *Proc. ACM MM*.
- [14] Alexey Dosovitskiy, Lucas Beyer, Alexander Kolesnikov, Dirk Weissenborn, Xiaohua Zhai, Thomas Unterthiner, Mostafa Dehghani, Matthias Minderer, Georg Heigold, Sylvain Gelly, et al. 2020. An Image is Worth 16x16 Words: Transformers for Image Recognition at Scale. In *Proc. ICLR*.
- [15] Zhenxuan Fang, Fangfang Wu, Weisheng Dong, Xin Li, Jinjian Wu, and Guangming Shi. 2023. Self-supervised Non-uniform Kernel Estimation with Flow-based Motion Prior for Blind Image Deblurring. In *Proc. CVPR*.
- [16] Hu Gao and Depeng Dang. 2024. Learning Enriched Features via Selective State Spaces Model for Efficient Image Deblurring. *arXiv preprint arXiv:2403.20106* (2024).
- [17] Jun Guo and Hongyang Chao. 2016. Building Dual-Domain Representations for Compression Artifacts Reduction. In *Proc. ECCV*.
- [18] Shaojie Guo, Haoifei Song, Qingli Li, and Yan Wang. 2024. Spatially-Variant Degradation Model for Dataset-free Super-resolution. *arXiv preprint arXiv:2407.08252* (2024).
- [19] Chi Han, Mingxuan Wang, Heng Ji, and Lei Li. 2021. Learning shared semantic space for speech-to-text translation. *arXiv preprint arXiv:2105.03095* (2021).
- [20] Ronghang Hu, Amanpreet Singh, Trevor Darrell, and Marcus Rohrbach. 2020. Iterative Answer Prediction With Pointer-Augmented Multimodal Transformers for TextVQA. In *Proc. CVPR*.
- [21] Insoo Kim, Jae Seok Choi, Geonseok Seo, Kinam Kwon, Jinwoo Shin, and Hyong-Euk Lee. 2024. Real-World Efficient Blind Motion Deblurring via Blur Pixel Discretization. In *Proc. CVPR*.
- [22] Taewoo Kim, Hoonhee Cho, and Kuk-Jin Yoon. 2024. Frequency-aware Event-based Video Deblurring for Real-World Motion Blur. In *Proc. CVPR*. 24966–24976.
- [23] Lingshun Kong, Jiangxin Dong, Jianjun Ge, Mingqiang Li, and Jinshan Pan. 2023. Efficient Frequency Domain-based Transformers for High-Quality Image Deblurring. In *Proc. CVPR*.
- [24] Lingshun Kong, Jiangxin Dong, Ming-Hsuan Yang, and Jinshan Pan. 2024. Efficient Visual State Space Model for Image Deblurring. *arXiv preprint arXiv:2405.14343* (2024).
- [25] Orest Kupyn, Volodymyr Budzan, Mykola Mykhailych, Dmytro Mishkin, and Jiri Matas. 2018. DeblurGAN: Blind Motion Deblurring Using Conditional Adversarial Networks. In *Proc. CVPR*.
- [26] Orest Kupyn, Tetiana Martyniuk, Junru Wu, and Zhangyang Wang. 2019. DeblurGAN-v2: Deblurring (Orders-of-Magnitude) Faster and Better. In *Proc. ICCV*.
- [27] Ao Li, Le Zhang, Yun Liu, and Ce Zhu. 2023. Feature Modulation Transformer: Cross-Refinement of Global Representation via High-Frequency Prior for Image Super-Resolution. In *Proc. ICCV*.
- [28] Jingyun Liang, Jiezhang Cao, Guolei Sun, Kai Zhang, Luc Van Gool, and Radu Timofte. 2021. SwinIR: Image Restoration Using Swin Transformer. In *Proc. ICCV Workshop*.
- [29] Chengxu Liu, Xuan Wang, Xiangyu Xu, Ruhao Tian, Shuai Li, Xueming Qian, and Ming-Hsuan Yang. 2024. Motion-adaptive Separable Collaborative Filters for Blind Motion Deblurring. In *Proc. CVPR*.
- [30] Ze Liu, Yutong Lin, Yue Cao, Han Hu, Yixuan Wei, Zheng Zhang, Stephen Lin, and Baining Guo. 2021. Swin Transformer: Hierarchical Vision Transformer using Shifted Windows. In *Proc. ICCV*.
- [31] Ze Liu, Yutong Lin, Yue Cao, Han Hu, Yixuan Wei, Zheng Zhang, Stephen Lin, and Baining Guo. 2021. Swin Transformer: Hierarchical Vision Transformer using Shifted Windows. In *Proc. ICCV*.
- [32] Ilya Loshchilov and Frank Hutter. 2017. SGDR: Stochastic Gradient Descent with Warm Restarts. In *Proc. ICLR*.
- [33] Xiaoqian Lv, Shengping Zhang, Chenyang Wang, Yichen Zheng, Bineng Zhong, Chongyi Li, and Liqiang Nie. 2024. Fourier Priors-Guided Diffusion for Zero-Shot Joint Low-Light Enhancement and Deblurring. In *Proc. CVPR*.
- [34] Xintian Mao, Qingli Li, and Yan Wang. 2024. AdaRevD: Adaptive Patch Exiting Reversible Decoder Pushes the Limit of Image Deblurring. In *Proc. CVPR*.
- [35] Xintian Mao, Yiming Liu, Fengze Liu, Qingli Li, Wei Shen, and Yan Wang. 2023. Intriguing Findings of Frequency Selection for Image Deblurring. In *Proc. AAAI*.
- [36] Sun Mengdi, Xiaohai He, Xiong Shuhua, Chao Ren, and Li Xinglong. 2020. Reduction of JPEG compression artifacts based on DCT coefficients prediction. *Neurocomputing* (2020).
- [37] Seungjun Nah, Tae Hyun Kim, and Kyoung Mu Lee. 2017. Deep Multi-scale Convolutional Neural Network for Dynamic Scene Deblurring. In *Proc. CVPR*.
- [38] Seungjun Nah, Sanghyun Son, Suyoung Lee, Radu Timofte, and Kyoung Mu Lee. 2021. NTIRE 2021 Challenge on Image Deblurring. In *Proc. CVPR Workshop*.
- [39] Zequn Qin, Pengyi Zhang, Fei Wu, and Xi Li. 2020. FcaNet: Frequency Channel Attention Networks. In *Proc. ICCV*.
- [40] Yongming Rao, Wenliang Zhao, Zheng Zhu, Jiwen Lu, and Jie Zhou. 2021. Global Filter Networks for Image Classification. In *Proc. NeurIPS*.
- [41] Jaesung Rim, Haeyun Lee, Jucheol Won, and Sunghyun Cho. 2020. Real-World Blur Dataset for Learning and Benchmarking Deblurring Algorithms. In *Proc. ECCV*.
- [42] Oren Rippel, Jasper Snoek, and Ryan P. Adams. 2015. Spectral Representations for Convolutional Neural Networks. In *Proc. NeurIPS*.
- [43] Olaf Ronneberger, Philipp Fischer, and Thomas Brox. 2015. U-Net: Convolutional Networks for Biomedical Image Segmentation. In *Proc. MICCAI*.
- [44] Jie Shao, Xin Wen, Bingchen Zhao, and Xiangyang Xue. 2021. Temporal Context Aggregation for Video Retrieval With Contrastive Learning. In *Proc. WACV*. 3268–3278.
- [45] Jiwei Shen, Pengjie Lou, Liang Yuan, Shujing Lyu, and Yue Lu. 2024. VME-Transformer: Enhancing Visual Memory Encoding for Navigation in Interactive Environments. *IEEE Robotics and Automation Letters* 9, 1 (2024), 643–650. <https://doi.org/10.1109/LRA.2023.3333238>
- [46] Ziyi Shen, Wenguan Wang, Xiankai Lu, Jianbing Shen, Haibin Ling, Tingfa Xu, and Ling Shao. 2019. Human-Aware Motion Deblurring. In *Proc. ICCV*.
- [47] Haoifei Song, Xintian Mao, Jing Yu, Qingli Li, and Yan Wang. 2024. I 3 Net: Inter-Intra-slice Interpolation Network for Medical Slice Synthesis. *IEEE Transactions on Medical Imaging* (2024).
- [48] Weijie Su, Xizhou Zhu, Yue Cao, Bin Li, Lewei Lu, Furu Wei, and Jifeng Dai. 2020. VL-BERT: Pre-training of Generic Visual-Linguistic Representations. In *Proc. ICLR*.
- [49] Chen Sun, Austin Myers, Carl Vondrick, Kevin Murphy, and Cordelia Schmid. 2019. VideoBERT: A Joint Model for Video and Language Representation Learning. In *Proc. ICCV*. 7463–7472.
- [50] Roman Suvorov, Elizaveta Logacheva, Anton Mashikhin, Anastasia Remizova, Arsenii Ashukha, Aleksei Silvestrov, Naejin Kong, Harshith Goka, Kiwoong Park, and Victor Lempitsky. 2022. Resolution-robust Large Mask Inpainting with Fourier Convolutions. In *Proc. WACV*.
- [51] Xin Tao, Hongyun Gao, Xiaoyong Shen, Jue Wang, and Jiaya Jia. 2018. Scale-Recurrent Network for Deep Image Deblurring. In *Proc. CVPR*.
- [52] Fu-Jen Tsai, Yan-Tsung Peng, Yen-Yu Lin, Chung-Chi Tsai, and Chia-Wen Lin. 2022. Stripformer: Strip Transformer for Fast Image Deblurring. In *Proc. ECCV*.
- [53] Zhengzhong Tu, Hossein Talebi, Han Zhang, Feng Yang, Peyman Milanfar, Alan Bovik, and Yinxiao Li. 2022. MAXIM: Multi-Axis MLP for Image Processing. In *Proc. CVPR*.
- [54] Ashish Vaswani, Noam Shazeer, Niki Parmar, Jakob Uszkoreit, Llion Jones, Aidan N Gomez, Łukasz Kaiser, and Illia Polosukhin. 2017. Attention is all you need. In *Proc. NeurIPS*.

- [55] Zhendong Wang, Xiaodong Cun, Jianmin Bao, and Jianzhuang Liu. 2022. Uformer: A General U-Shaped Transformer for Image Restoration. In *Proc. CVPR*.
- [56] Jay Whang, Mauricio Delbracio, Hossein Talebi, Chitwan Saharia, Alexandros G. Dimakis, and Peyman Milanfar. 2022. Deblurring via Stochastic Refinement. In *Proc. CVPR*.
- [57] Wenbin Xie, Dehua Song, Chang Xu, Chunjing Xu, Hui Zhang, and Yunhe Wang. 2021. Learning Frequency-Aware Dynamic Network for Efficient Super-Resolution. In *Proc. ICCV*.
- [58] Yanchao Yang and Stefano Soatto. 2020. FDA: Fourier Domain Adaptation for Semantic Segmentation. In *Proc. CVPR*.
- [59] Ting Yao, Yingwei Pan, Yehao Li, Chong-Wah Ngo, and Tao Mei. 2022. Wave-ViT: Unifying Wavelet and Transformers for Visual Representation Learning. In *Proc. ECCV*.
- [60] Hu Yu, Jie Huang, Feng Zhao, Jinwei Gu, Chen Change Loy, Deyu Meng, Chongyi Li, et al. 2022. Deep Fourier Up-Sampling. In *Proc. NeurIPS*.
- [61] Boxiang Yun, Xingran Xie, Qingli Li, and Yan Wang. 2023. Uni-Dual: A Generic Unified Dual-Task Medical Self-Supervised Learning Framework. In *Proc. ACM MM*. 3887–3896.
- [62] Syed Waqas Zamir, Aditya Arora, Salman H. Khan, Munawar Hayat, Fahad Shahbaz Khan, and Ming-Hsuan Yang. 2022. Restormer: Efficient Transformer for High-Resolution Image Restoration. In *Proc. CVPR*.
- [63] Syed Waqas Zamir, Aditya Arora, Salman H. Khan, Munawar Hayat, Fahad Shahbaz Khan, Ming-Hsuan Yang, and Ling Shao. 2021. Multi-Stage Progressive Image Restoration. In *Proc. CVPR*.
- [64] Hongguang Zhang, Yuchao Dai, Hongdong Li, and Piotr Koniusz. 2019. Deep Stacked Hierarchical Multi-Patch Network for Image Deblurring. In *Proc. CVPR*.
- [65] Kaihao Zhang, Wenhan Luo, Yiran Zhong, Lin Ma, Björn Stenger, Wei Liu, and Hongdong Li. 2020. Deblurring by Realistic Blurring. In *Proc. CVPR*.
- [66] Bolun Zheng, Shanxin Yuan, Chenggang Yan, Xiang Tian, Jiyong Zhang, Yaoqi Sun, Lin Liu, Aleš Leonardis, and Gregory Slabaugh. 2022. Learning Frequency Domain Priors for Image Demoiréing. *IEEE Transactions on Pattern Analysis and Machine Intelligence* 44, 11 (2022), 7705–7717. <https://doi.org/10.1109/TPAMI.2021.3115139>
- [67] Yijie Zhong, Bo Li, Lv Tang, Senyun Kuang, Shuang Wu, and Shouhong Ding. 2022. Detecting Camouflaged Object in Frequency Domain. In *Proc. CVPR*.
- [68] Zhisheng Zhong, Tiancheng Shen, Yibo Yang, Zhouchen Lin, and Chao Zhang. 2018. Joint Sub-bands Learning with Clique Structures for Wavelet Domain Super-Resolution. In *Proc. NeurIPS*.

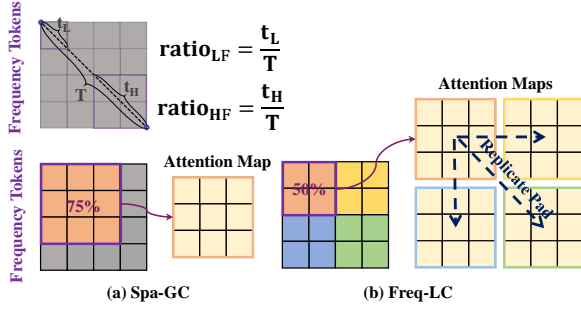


Figure 9: Detailed illustration for Fig. 8 in the main body of the paper. For the feature in the frequency domain, we take the diagonal line as the axis of proportional selection. For the frequency feature $X \in \mathbb{R}^{H \times W}$, the points on the diagonal line is used to define the range of low / high frequency (LF/HF). Take the point $X_{h,w}$ located in $[h, w]$ as an example, the attention map with LF/HF ratio ($\text{ratio}_{\text{LF}} / \text{ratio}_{\text{HF}}$) is done in the set of $X_{i,j}$, where $i < h$ and $j < w$ (LF), $i \geq h$ and $j \geq w$ (HF). $\text{ratio}_{\text{LF}} = \frac{t_L}{T}$, $\text{ratio}_{\text{HF}} = \frac{t_H}{T}$, where $t_L = \sqrt{h^2 + w^2}$, $t_H = \sqrt{(H-h)^2 + (W-w)^2}$, $T = \sqrt{H^2 + W^2}$. For Freq-LC, we draw local windows with the window size $b = 2$ for simplicity.

A Detailed Illustration on the Horizontal Axis of Fig. 8 in the Main Paper

In Fig. 8 of the main paper, we show Spa-GC-LF/HF and Freq-LC-LF/HF. Here we illustrate how to compute the frequency ratio on the horizontal axis.

As the purple boxes shown in Fig. 9, the frequency ratio for LF/HF is determined by the diagonal length of LF/HF box *w.r.t.* the diagonal length of the feature map. See $\text{ratio}_{\text{LF}} = \frac{t_L}{T}$, $\text{ratio}_{\text{HF}} = \frac{t_H}{T}$ in the top figure of Fig. 9.

For Spa-GC, we take 75% LF as an example in Fig. 9 (a), the channel-wise attention map is simply calculated on features inside 75% LF purple box. The cosine similarity of Spa-GC in the right figure in Fig. 8 in the main paper is calculated between the source attention map with different ratios of LF/HF and the target attention map with all the information.

For our Freq-LC, when including whole frequency information, we can get attention maps $\tilde{A} \in \mathbb{R}^{m \times C \times C}$. When executing Freq-LC by a percentage ($p \in (0, 1]$) of LF/HF, we get partial attention maps $\tilde{A}^* \in \mathbb{R}^{p^2 \times m \times C \times C}$. To complete attention maps with size $m \times C \times C$, replicate padding is adopted to pad the rest attention maps. We take 50% LF as an example for Freq-LC-LF in Fig. 9 (b).

B Attention Maps

To better understand whether the attention maps learned from each local window are the same or different, we calculate the Cosine Similarity matrices of the attention maps in stage-1. As shown in Fig. 10, the attention maps in Freq-GC (32.84dB) are similar to each other, which suppresses the network’s learning ability for high-frequency (fine) information. While the attention maps in Freq-LC (33.17dB) are quite different from each other, indicating

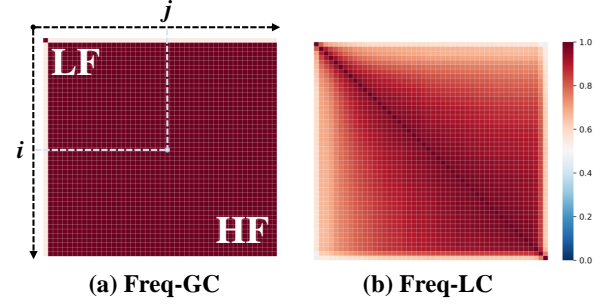


Figure 10: Cross cosine similarity among attention maps of different windows along the diagonal line in Stage-1. For example, the value in position (i, j) means the cosine similarity between $\tilde{A}^{i,i}$ and $\tilde{A}^{j,j}$, where $i \in \mathbb{R}^{H/b}$, $j \in \mathbb{R}^{W/b}$ and $\tilde{A} \in \mathbb{R}^{H/b \times W/b \times C \times C}$.



Figure 11: Images with different low-frequency ratios. Almost all the energy lies in the low frequency which represents the structure of the image.

that different independent local windows provide information in different ways for image deblurring.

C Images with Different Low-frequency Ratios

We provide the images with various ratios of LF in Fig. 11. As is indicated in Fig. 11, almost all the energy lies in LF, which dominates the calculation of Spa-GC.

D Visual Results

The visual results on GoPro [37], HIDE [46], RealBlur-R [41], RealBlur-J [41] and REDS [38] are shown in Fig. 12- 17. Our model yields more visually pleasant outputs than other methods on both synthetic / real-world motion deblurring. Compared with NAFNet64 [4], which has a competitive performance on GoPro dataset, Fig. 14 shows that LoFormer is much more robust than NAFNet64.

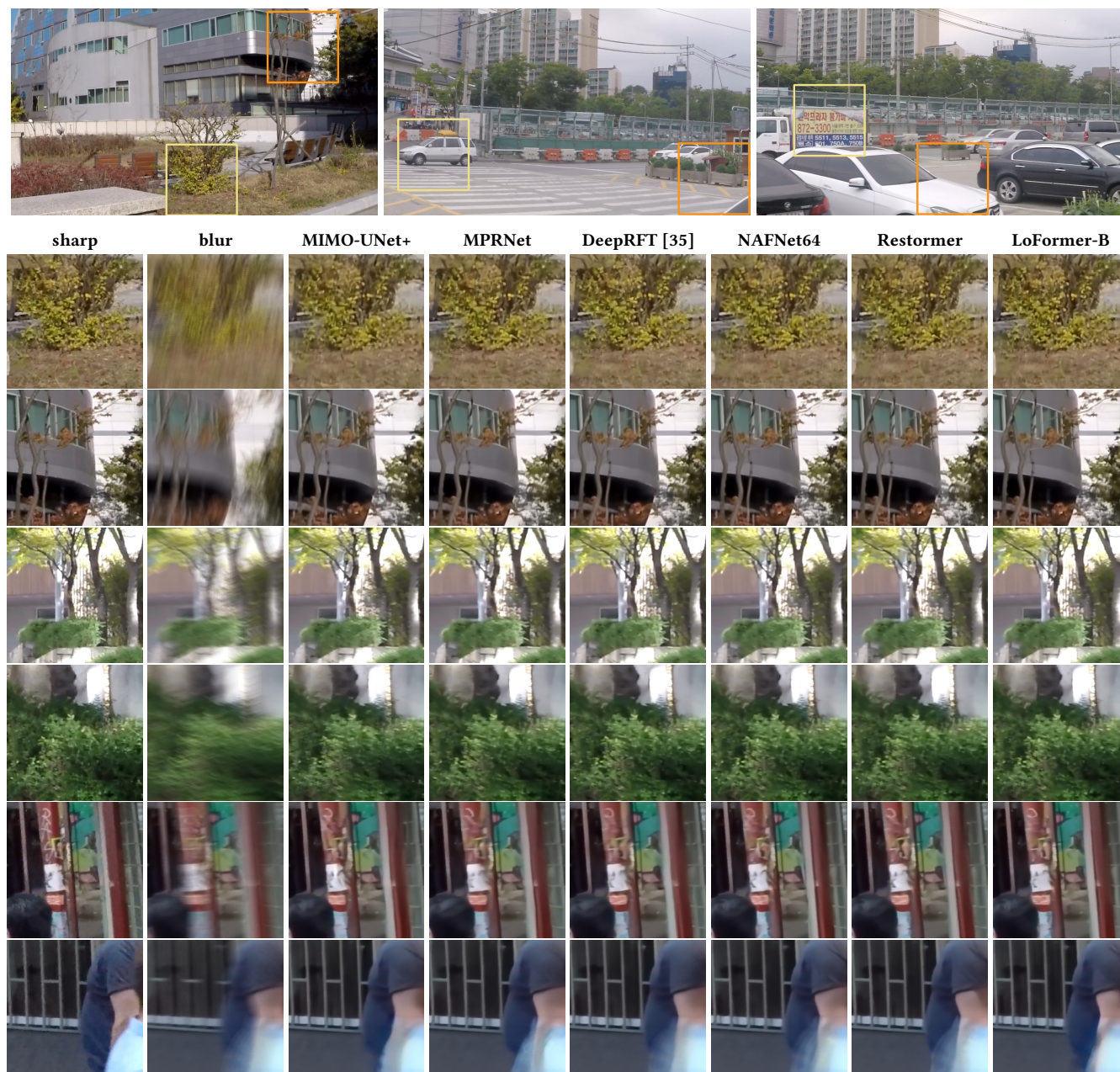


Figure 12: Examples on the GoPro test set.

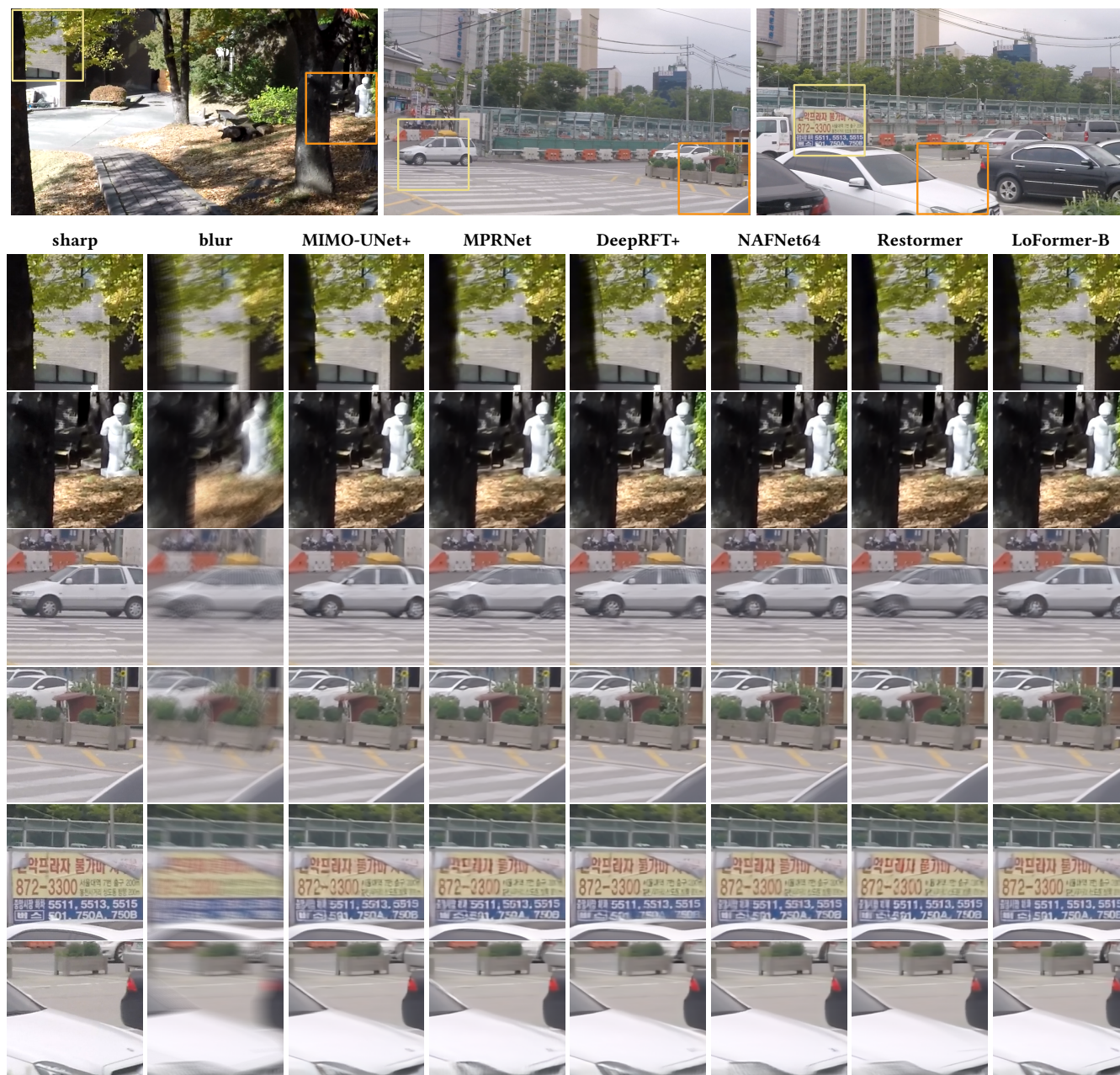


Figure 13: Examples on the GoPro test set.

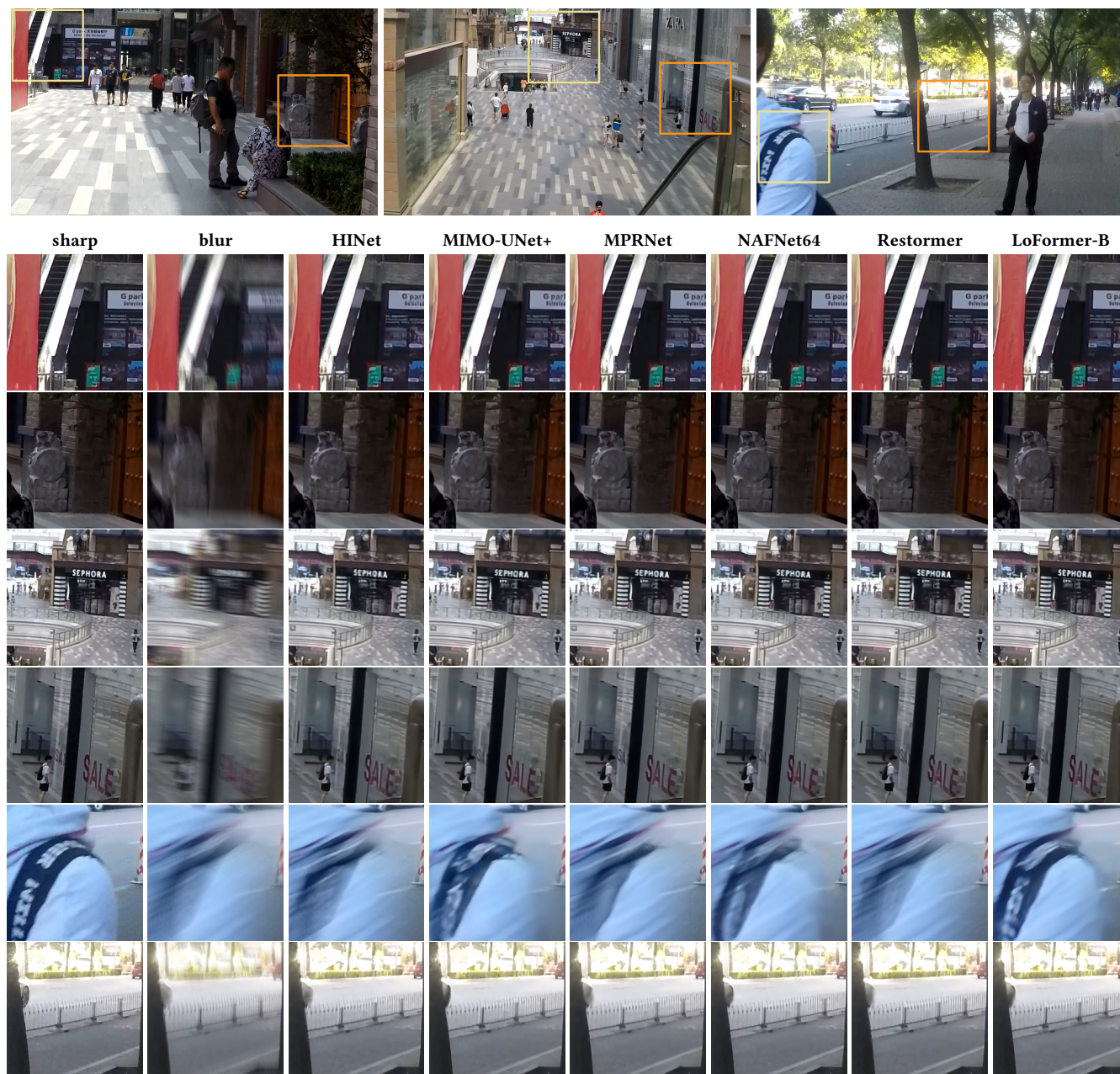


Figure 14: Examples on the HIDE test set.

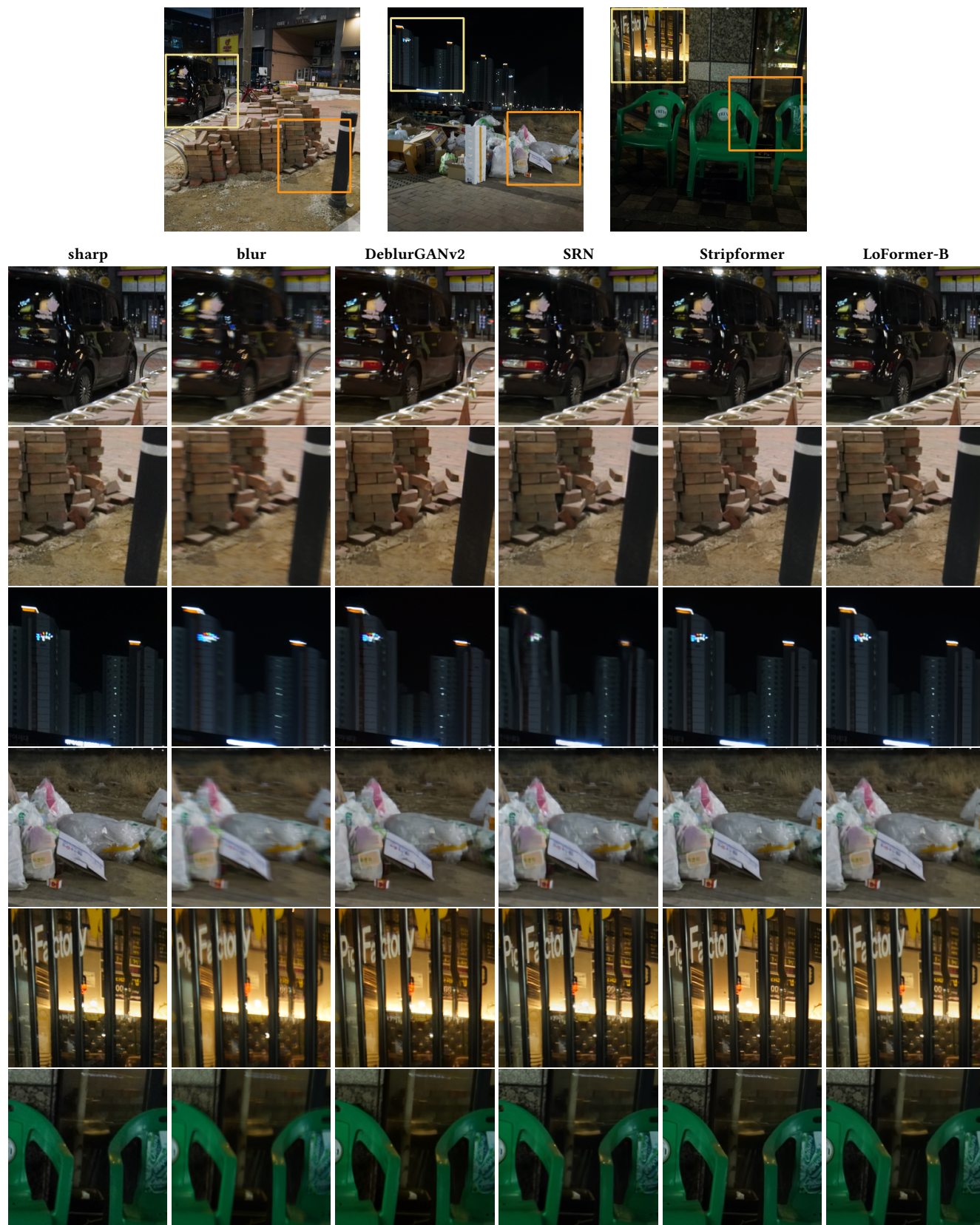


Figure 15: Examples on the RealBlur-J test set.

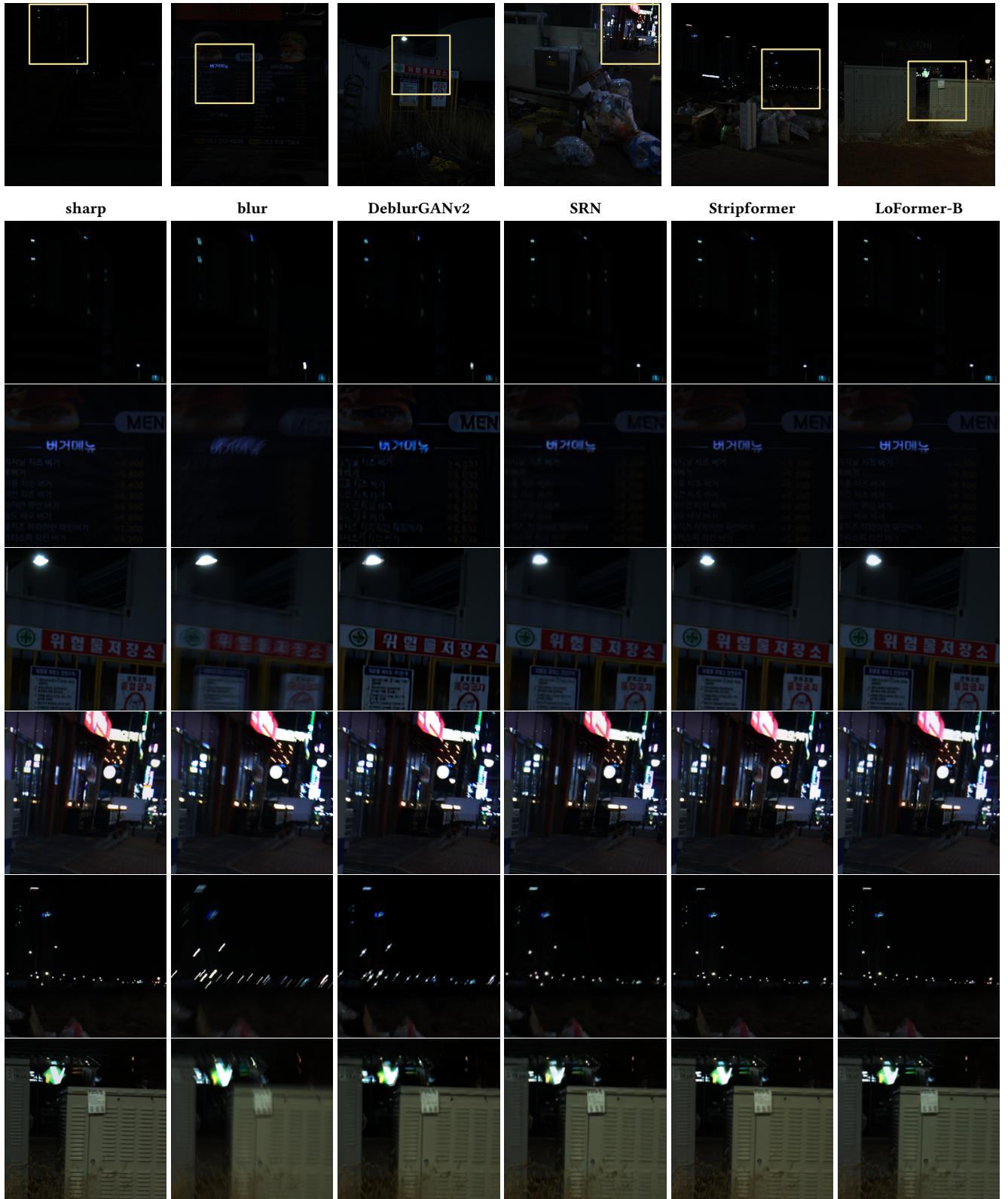


Figure 16: Examples on the RealBlur-R test set.

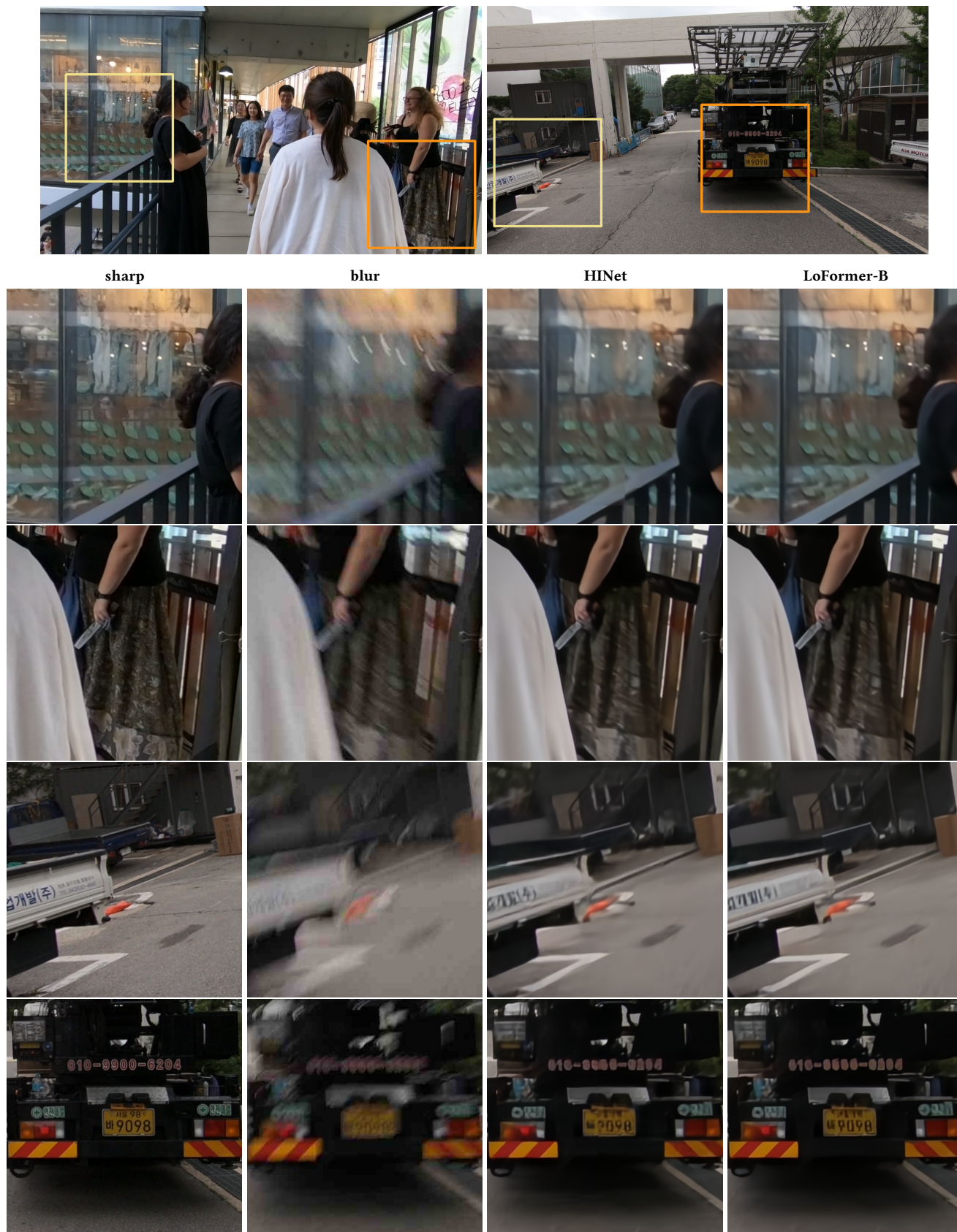


Figure 17: Examples on the REDS-val-300 set.